Journal of Colloid and Interface Science 679 (2025) 324–333

Contents lists available at ScienceDirect

Journal of Colloid And Interface Science

journal homepage: www.elsevier.com/locate/jcis

Regular Article

Self-stratification and phase separation in drying binary colloidal films

Ellard Hooiveld [a], Lisa Rijnders [a], Berend van der Meer [a], Jasper van der Gucht [a], Joris Sprakel [b], Hanne M. van der Kooij [a,*]

[a] Physical Chemistry and Soft Matter, Wageningen University & Research, Stippeneng 4, Wageningen, 6708 WE, the Netherlands
[b] Laboratory of Biochemistry, Wageningen University & Research, Stippeneng 4, Wageningen, 6708 WE, the Netherlands

GRAPHICAL ABSTRACT

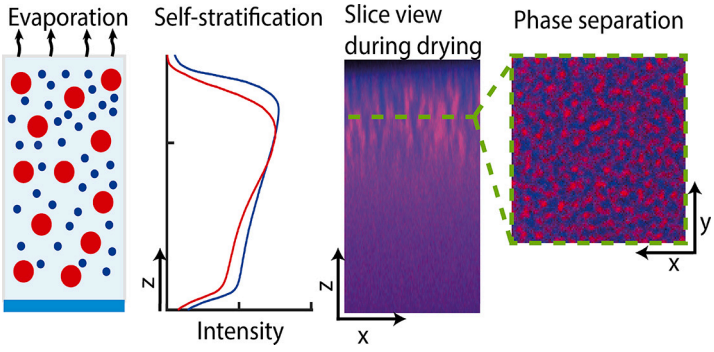

ARTICLE INFO

Keywords:
Multi-component coatings
Binary colloidal films
Phase separation
Stratification
Dispersion drying
In-situ confocal imaging
Diffusiophoresis
Non-equilibrium thermodynamics

ABSTRACT

Hypothesis: Films that develop compositional heterogeneity during drying offer a promising approach for achieving tailored functionalities. These functionalities can be realized by strategically directing different components during the drying process. One approach to achieve this is through spontaneous size segregation of colloidal particles. Two variants thereof have previously been observed in binary suspensions: layer formation (self-stratification) due to kinetically driven concentration gradients, and micro-domain formation (phase separation) due to thermodynamic depletion interactions between the small and large species. Surprisingly, in the context of binary colloidal films, these phenomena have never been investigated concurrently during evaporation.
Experiments: We show how we can achieve both self-stratification and domain formation in a single step. Using real-time 3D confocal fluorescence microscopy, we quantitatively unravel the effects of various parameters on the emergence of compositional heterogeneity.
Findings: We reveal that beyond a certain size ratio, micro-phase separation becomes a prominent mechanism dictating the final morphology. The initial volume fraction minimally affects the final domain size but significantly impacts self-stratification. Reducing the evaporation rate increases the domain size while minimizing stratification. Finally, reducing the colloidal electrostatic interaction by a small increase in salt concentration enhances phase separation yet reverses stratification. These findings unveil a strategy for harnessing two distinct size segregation mechanisms in a single film, forming a foundation for customizable self-partitioning coatings.

* Corresponding author.
E-mail address: Hanne.vanderKooij@wur.nl (H.M. van der Kooij).

https://doi.org/10.1016/j.jcis.2024.10.102
Received 12 August 2024; Received in revised form 30 September 2024; Accepted 17 October 2024
Available online 21 October 2024

1. Introduction

The drying of colloidal mixtures is a prevalent occurrence across numerous industries, including cosmetics, paints [1], (bio-)coatings [2], inks [3] and foods [4–6]. Multiple colloidal species are often combined to create a final dried film with enhanced attributes and a multitude of functions, such as adhesion to the substrate [7], colour, gloss, electrical conductivity [8], abrasion resistance [9], UV resistance or anti-fouling. These functionalities are closely tied to the particle distribution within the dry film. Before application, the colloidal mixtures are typically homogeneous. However, the intricate interplay between diffusion, fluid flows, and colloidal interactions during drying can disrupt the homogeneity of the mixture [10]. This often results in (partial) demixing of the colloids as the solvent evaporates [2,7,9,11,12]. In some cases, such separation is disadvantageous, but it can also offer opportunities to strategically position different particle populations. Typically, the positioning of particles involves the sequential addition of different layers, a process that is both time-consuming and energy-intensive. Self-structuring during drying offers a promising and sustainable alternative. To illustrate, it allows the creation of layered structures with specific properties: anti-fouling and anti-scratch colloids can be positioned near the air interface, while anti-corrosive and adhesive particles can be placed near the substrate. To effectively guide the demixing of colloidal particles during evaporation, various segregation pathways need to be considered.

For example, a binary colloidal mixture, consisting of colloids with two different sizes, can autonomously separate into different layers during drying, also known as self-stratification or auto-stratification [13]. In the colloidal regime, where gravity does not lead to particle sedimentation or creaming [14], self-stratification can yield two distinct structural outcomes. (1) When the rate of evaporation substantially outpaces the time required for homogenization of the large particles, due to their slow diffusion, the larger particles become kinetically trapped beneath the evaporating surface, while the more swiftly diffusing smaller particles maintain a homogeneous distribution within the film. This culminates in the formation of a 'large-on-top' stratified structure [15]. (2) If both types of particles are entrapped by the evaporation interface, this results in the emergence of steep concentration gradients of both species. In this scenario, the pronounced concentration gradient of the smaller particles prompts the displacement of larger particles away from the evaporation interface, driven by a phenomenon called diffusiophoresis. This effect arises from the asymmetrical interactions between small and large particles, stemming from differences in their respective volumes. Consequently, so-called 'small-on-top' stratification ensues [13,16,17]. Both of these demixing mechanisms are rooted in the non-equilibrium state of the drying suspension, with separation primarily originating from the buildup of concentration gradients throughout the evaporation process and the asymmetric particle-particle interactions [18–20].

In recent years, extensive experimental, theoretical and numerical research has been conducted to investigate the mechanisms leading to self-stratification, with a wide array of parameters including particle sizes [18,19,21–23], particle interactions [23–26], initial volume fractions [25,27], solvent viscosity [28,29], evaporation speed, [30] temperature [31] and humidity [32]. These studies focus mainly on the buildup of vertical concentration gradients leading to stratification, but they overlook the possibility of thermodynamic demixing as the particle concentration increases.

As evaporation advances, the increasing particle concentrations will modify the thermodynamic equilibrium conditions of the system, possibly affecting its homogeneity. Many studies have demonstrated that in undisturbed (non-evaporating) binary colloidal mixtures with varying sizes, phase separation can initiate due to depletion interactions [33–37]. Depletion flocculation occurs due to the notion that when the large particles cluster together, they create additional free space for the small particle type. This phenomenon increases the configurational entropy, thereby reducing the overall free energy of the system. The system will start to phase separate above a critical volume fraction of the particles [35]. This phase separation can be equilibrium or non-equilibrium in nature [38]. During this process, domains of different composition first emerge through nucleation or spinodal decomposition, and subsequently grow in size through a coarsening process. Notably, this critical volume fraction diminishes with an increasing size ratio between the particles [31,33].

Surprisingly, for films, such evaporation-induced phase separation has not been studied before, although binary colloidal suspensions may well cross the critical volume fraction during drying [31]. This has been shown for evaporating binary polymer systems mixtures [39,40]. The resultant polymer or colloidal clustering has the potential to form a variety of microstructures [39,41], which could significantly influence the final macroscopic properties of the dry film, whether desired or undesired [11].

Both diffusiophoretic and phase separation pathways could be harnessed to tune the composition of a binary colloidal mixture during evaporation. The diffusiophoretic pathway allows for vertical segregation relative to the evaporation front, while phase separation adds an extra degree of freedom, enabling the steering of particle distribution in a three-dimensional manner. The entropy-driven nature of depletion interactions renders this mode of material structurization broadly applicable to any colloidal dispersion of size-asymmetric particles. However, the combined action of these pathways remains elusive.

In this research, we explore the concerted interplay between diffusiophoretic and phase separation processes involved during the drying of a binary suspension film. Using 3D confocal microscopy and quantitative image analysis, we precisely track the distribution of fluorescently labelled particles in situ [25]. This approach allows us to quantitatively observe stratification and phase separation domain size in real-time during the evaporation. We show that size ratio, initial volume fractions, evaporation speed, and effective particle interaction distance highly effect both phenomena. The interplay between these pathways ultimately determines the composition of the final dry film, thereby dictating its properties. Understanding these processes is crucial for designing single-deposition films with bespoke partitioning patterns.

2. Materials and methods

2.1. Materials

A 76:24 (v/v) mixture of *tert*-butyl methacrylate (tBMA, TCI, >98.0%, MEHQ stabilized) and 2,2,2-trifluoroethyl methacrylate (TFEMA, TCI, >98.0%, MEHQ stabilized) was made and will be referred to as tBMA/TFEMA mixture. Formamide (98.5%) was obtained from TCI. Sodium dodecyl sulfate (SDS, for synthesis), potassium peroxodisulfate (KPS, >99.0%) and *trichloro(1H,1H,2H,2H-perfluorooctyl)silane* (97%) were purchased from Sigma-Aldrich. The fluorescent dyes pyrromethene 546 (PM546, laboratory use) and pyrromethene 650 (PM650, laboratory use) were purchased from Exciton. Polydimethylsiloxane (PDMS, Sylgard 184) base and curing Agent were obtained from Dow. All chemicals were used without extra purification.

2.2. Particle synthesis and characterizations

Colloids were synthesized via emulsion polymerization, employing varying quantities of surfactant to control the final particle size [42,43]. A monomer blend comprising 2,2,2-trifluoroethyl methacrylate and *tert*-butyl methacrylate (76:24 v/v) was selected to ensure density and refractive index matching with the solvent, formamide [44]. Fluorescent labelling was achieved using pyrromethene 546 (PM546) or pyrromethene 650 (PM650) for the small and large particles, respectively. Detailed protocols can be found in the Supplementary Material.

The hydrodynamic diameters of the particles (D_h) were characterized using dynamic light scattering (DLS). These measurements were

performed on an ALV instrument equipped with an ALV-7002 external correlator and a 380 mW Cobolt Flamenco-300 laser operating at a wavelength of 660 nm. A very diluted dispersion of particles in Milli-Q water was measured in polycarbonate capillaries of 1.9 mm diameter (Enki SRL) at a detection angle of 90° and a temperature of 20 °C. The stability of the particles was checked by with similar DLS measurements in 1 mM, 10 mM, 50 mM and 250 mM KCl (the refractive index matching is not perfect allowing for DLS measurements) in formamide at 25 °C. The small particles where diluted to 0.2 Wt % and the large particles to 0.075 Wt %. A CONTIN analysis was conducted on the decay curves to give a size distribution.

To match the density and refractive index of the particles with the solvent, the water was replaced by formamide via dialysis. A Spectra/Por 3 Dialysis membrane standard RC tubing of 3.5 kD was loaded with 10-50 mL particle dispersion, and the dispersion was dialysed against 500 g formamide for several days. Hereafter, the particle suspensions were transparent, due to the refractive index match between the particles and formamide. For the experiments at different salt concentrations, approximately 15 mL of colloidal suspensions, spanning various salt concentrations, underwent initial dialysis for 7 days against 5 L of Milli-Q water, with daily refreshing of the Milli-Q water. Subsequently, they underwent dialysis against pure formamide containing either 1 mM, 10 mM, or 50 mM KCl. Although the water could not be fully replaced by formamide, the dispersions became transparent and allowed for good confocal measurements. The weight fractions of the dispersions were determined gravimetrically by evaporating the formamide overnight at 114 ˚C. No particle sedimentation or creaming was observed for both particle types in formamide, even after two months of storage. These dispersions were then blended and diluted with formamide to form the initial binary colloidal suspensions. The bulk viscosity of these samples was measured by placing a 5 mL glass pipette vertically and recording the time it took for 3 mL to drain. The drainage times were then compared to those of pure formamide (η_0) to calculate the viscosity increase factor: $\eta_r = \frac{\eta}{\eta_0}$.

Neither of the colloidal species exhibited measurable adsorption at the formamide–air interface. For experiments requiring different salt concentrations, formamide containing 1 mM, 10 mM, or 50 mM KCl was employed for dilution.

2.3. Glass modification

The glass plate designated for the confocal microscopy experiments was rendered hydrophobic by silane modification to prevent the coffee ring effect by decreasing the contact angle hysteresis [45]. This was done by adding a drop (20 µl) of 1% trichloro(1H,1H,2H,2H-perfluorooctyl)silane in isopropanol (IPA) to the glass surface. The IPA was allowed to evaporate for 1-2 minutes, and the remaining residue was gently removed by lightly dabbing the surface with a tissue, resulting in a modified glass surface. Between the different experiments, the surface was rinsed thoroughly with Milli-Q water and subsequently IPA and carefully wiped with a tissue soaked with acetone. Hereafter it was again rinsed with Milli-Q water. Finally, it was dried by blowing dry N_2 gas, before application of a new sample.

2.4. In-situ confocal microscopy

Various mixtures of the synthesized particles were prepared, as detailed in the Results and Discussion section. A 8-15 µl droplet was dispensed onto a 1 mm thick surface-modified glass slide within a custom design 3D printed vacuum chamber (**Fig. S1**) to create a thin film with a height ranging from approximately 600 to 900 µm. The droplet had an estimated contact angle of 80-90° and the signal was recorded at the center of the film, where top-down drying is most pronounced. The top of the vacuum chamber was closed using a PDMS slab (1:25 curing agent:base, cured for at least 2 h at 70 °C) and a glass slide (1 mm thick, ~ 40x20 mm). The evaporation of the formamide was initiated by creating a low-pressure environment between 5-35 mbar within the vacuum chamber. The evaporation of the formamide and its influence on the fluorescence intensities of the particle populations were followed using an inverted Nikon Eclipse Ti2 confocal laser scanning microscope and a 10× air objective (NA 0.45). The dye of the small particles, PM546, was excited at 488 nm, and fluorescence emission was detected within the range of 500 to 550 nm. The large particle dye PM650 was excited separately at 564 nm, and the emission was collected between 575 and 615 nm. Importantly, there was no significant cross-talk between these channels. Imaging was conducted using frames of 128×128 square pixels with a (digital) pixel size of 1.08 µm, covering the entire depth of the film with a z-step size of 3 µm. A single z-stack of both channels was acquired in approximately 9-14 min, depending on the height of the film. These confocal measurements were continued until the film had completely dried, with the exception of the slowly evaporating film.

2.5. Cross-section measurements

After evaporation, the films cracked, and flakes of the film could easily be removed since the surface modification prevented the dry films from sticking to the substrate. These flakes were positioned with the cross-section facing down for measurement on the confocal microscope. A fluorescence image of the cross-section of the film was then obtained using the same settings as above, yet with much higher resolution (pixel size between 0.04-0.25 µm). For scanning electron microscopy (SEM) measurements, the cross-sections were attached to an aluminum 90° SEM stub (Agar scientific, 12.7 mm diameter, 45/90° chamber, 9.5 mm pin) using electrically conductive and adhesive carbon tabs (EMS Washington USA). The cross-sections were sputter-coated 2× at an angle of 45° with 4 nm tungsten (MED 020 sputter-coater, Leica, Vienna, Austria). Between the two sputter-coatings, the sample was rotated laterally by 180° to ensure an even and uniform coating. This provided a conductive layer on top of the cross-sections. Hereafter, the samples were analyzed using a field emission electron microscope (Magellan 400, Thermo-Fisher/FEI, Eindhoven, the Netherlands) at 2 kV.

2.6. Image analysis

Image analysis and data processing were conducted using customized MATLAB scripts. These scripts covered tasks such as fluorescence intensity correction, determination of median values, analysis of intensity fluctuations, and distance correlation analysis. In the analysis, the focus remained exclusively on time points when the suspension had not completely dried and the fluorescence channels had not experienced overexposure of the fluorescent signal. A detailed explanation of these analyses can be found in the Supplementary Material.

3. Results and discussion

3.1. Real-time confocal microscopy of stratification and phase separation

Controlled size segregation of colloidal particles during drying offers a promising route for tailoring functionalities within films. To achieve real-time visualization of these size segregation processes in 3D, we employ confocal fluorescence microscopy on binary colloidal dispersions, where the two particles species are tagged with dissimilar fluorescent dyes, each possessing unique excitation and emission characteristics. This dual-labelling strategy allows us to track the fluorescence intensity of both species while the dispersant, formamide, evaporates (**Fig. 1a**). The particles are density-matched with the formamide, to avoid sedimentation or creaming, and refractive-index-matched, to reduce scattering. We start by drying a 800 µm thick film containing custom-synthesized small 55 nm particles and large 200 nm particles (see the Materials and Methods section), providing a size ratio of 3.6. The initial volume fraction of the small particles ($\phi_{S,0}$) is 0.12 and that of the large particles ($\phi_{L,0}$) is 0.024.

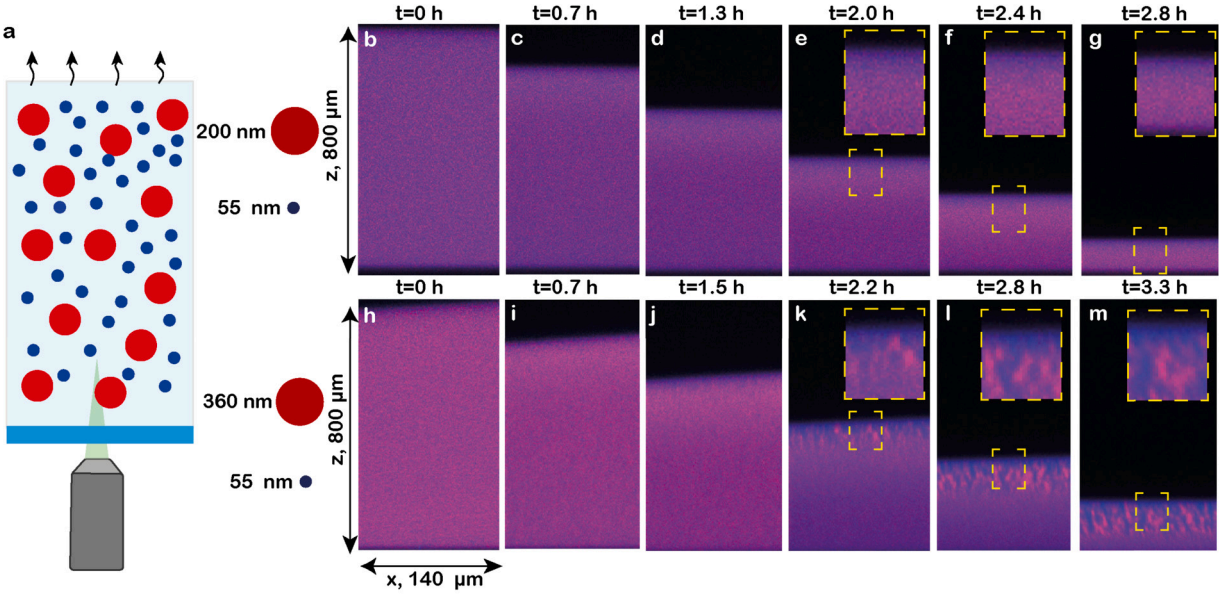

Fig. 1. Confocal microscopy of drying binary suspensions with colloids of different size ratios. (a) Schematic illustration of the experimental geometry. (b-m) xz fluorescence images for a size ratio of (b-g) 3.5 and (h-m) 6.5 at different time points as indicated. The small colloids are indicated in blue, and the large in red. An increased size ratio promotes both stratification and phase separation of the larger colloids into clusters. (For interpretation of the colours in the figure(s), the reader is referred to the web version of this article.)

Formamide evaporates effectively at low pressures (~ 10 mbar). This process is conducted in a custom-designed chamber that fits on the stage of a confocal microscope (**Fig. S1**). At the start of drying, the two colloidal species are spread evenly throughout the film (**Fig. 1b**). This homogeneity persists during the first two hours (**Fig. 1b-g**, **Video S1**). Once the film is approximately half way the drying process, we observe a slightly higher intensity of the small particles (blue) near the evaporation interface (**Fig. 1e**). This increased intensity remains throughout later drying stages, indicative of small-on-top stratification, a well-documented phenomenon [13]. Past research has shown that using a larger size ratio between the particles can lead to more pronounced size segregation [19,33]. Therefore, we increase the particle size ratio to 6.5 by using 360 nm large particles, with $\phi_{S,0}$ = 0.08 and $\phi_{L,0}$ = 0.04. At the start of evaporation, the colloids are uniformly mixed (**Fig. 1h-i**). After 1.5 h, similar to the previous sample, we find a discernible surplus of small particles persisting near the evaporation front, indicating small-on-top stratification. Below this layer after 2 h, we also observe a different form of segregation, in which the large particles cluster together, revealed by the high red intensities in the lateral direction (**Fig. 1k**, **Video S2**). Over time, these clusters expand and extend into deeper layers (**Fig. 1l-m**, **Fig. S2b**). The observed clustering is induced by the emergence of significant depletion forces arising due to the size disparity between the two species. A greater disparity in size lowers the critical volume fractions necessary for phase separation, indicating that phase separation is achievable only in samples with a significant size ratio [33]. Consequently, in this sample, we witness both vertical self-stratification, attributed to concentration gradients that arise during evaporation, and phase separation, driven by depletion interactions.

To validate and gain a more comprehensive view of these two demixing phenomena, we physically generate cross-sections of the films after drying and place them under the confocal microscope. In the dry film with the smaller size ratio of 3.5, only a gradual small-on-top stratification is observed, and no clear phase separation is visible (**Fig. S3a**). By contrast, the top of the film with the higher size ratio of 6.5 features a sharp narrow band comprised of small particles, unmistakably revealing the small-on-top stratification (**Fig. 2a**). Below this upper layer, fluctuations in intensity reveal domains that formed due to phase separation. To uncover the inner microstructure of these clusters, we zoom in on them using scanning electron microscopy (SEM), which confirms they are primarily composed of large particles (**Fig. 2b**, red demarcation). Notably, the phase dominant in large particles also contains a small proportion of smaller particles, and vice versa (**Fig. 2c**). These findings substantiate the coexistence of the two demixing phenomena observed in the time-resolved experiment.

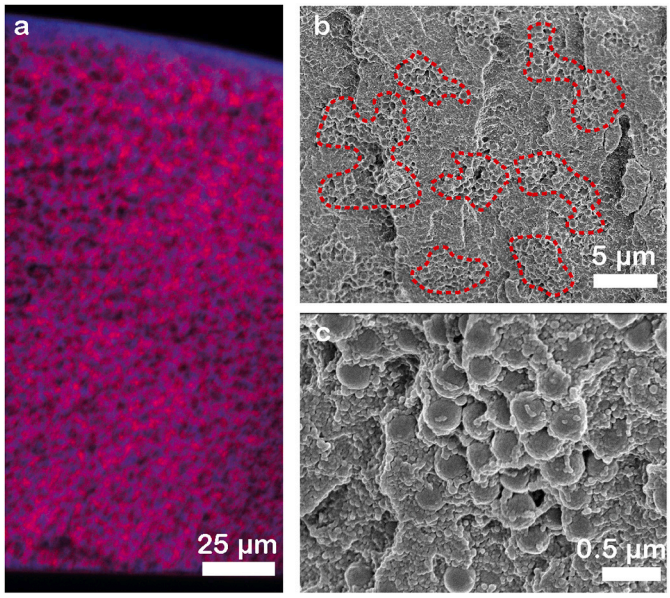

Fig. 2. Physically created cross-sections of a dry film with a particle size ratio of 6.5. (a) Confocal fluorescence micrograph. (b) SEM image taken far below the interface. Several phase separated large particle domains are outlined with red dashed lines. (c) Higher magnification SEM image of one such domain. These cross-sections unmistakably reveal that both stratification and phase separation play an important role for the final dry film composition.

3.2. *Effect of the initial concentration*

Having established the interplay between stratification and phase separation through control of the particle size ratio, we now turn to another critical parameter: the initial concentration. This parameter offers

a readily adjustable design lever for engineering the properties of the final film. We investigate binary mixtures with different initial volume fractions of small particles ($\phi_{S,0}$), while maintaining a constant volume fraction of the larger particles ($\phi_{L,0}$). It is well-established, based on both theoretical predictions and experiments, that this parameter can significantly influence the extent of self-stratification [19,46–48].

To gain a more quantitative insight into the stratification process, we calculate the median intensities along the z-direction of the fluorescence images ($< I_z >$). We additionally correct for fluorescence intensity loss, which inevitably occurs due to scattering and absorption effects in deeper layers (See **Fig. S4** and the Materials and Methods section). For identical $\phi_{L,0}$ and $\phi_{S,0}$ of 0.04 we observe a homogeneous mixture at the beginning of drying (**Fig. 3a**). As evaporation proceeds, both large and small particles progressively accumulate, revealed by the rising fluorescence intensity near the evaporation interface. These accumulations arise from the rapid propagation of the evaporation front compared to the diffusion of particles. The diffusion time required for particles to move from the top to the bottom of the film is proportional to $\frac{H^2}{D_i}$, where D_i represents the diffusion constant of the colloidal species i particle and H is the initial thickness of the film. The time required for complete evaporation of the dispersant is proportional to $\frac{H}{E}$ in which E is the evaporation speed. The ratio of these two time scales yields the Peclet number (Pe_i) for each colloidal species i:

$$Pe_i = \frac{H\,E}{D_i} \tag{1}$$

If $Pe \gg 1$, the colloids will accumulate near the top of the film while $Pe \ll 1$ leads to an even distribution of the particles throughout the film. [16,18,24,49,50] We determine H and E over time by computationally tracking the position of the evaporation front in the fluorescence intensity profiles (**Fig. S5b**). For our spherical particles, the Stokes–Einstein equation provides a first-order approximation of the diffusion constant:

$$D_i = \frac{k_B T}{6\pi\eta R_i} \tag{2}$$

where k_B is the Boltzmann constant, T is the temperature, η is the viscosity of formamide, and R_i is the radius of species i. Using H and E derived from our experimental data and D calculated according to **eq.** (2) we find $Pe_S = 20$ and $Pe_L = 123$ according to **eq.** (1) (**Tab S1**). These Peclet numbers $\gg 1$ confirm that the evaporation speed is much faster than the diffusion of the particles, giving rise to steep concentration gradients.

While both colloidal species accumulate near the drying interface, the fluorescence signal of the large particles is even more pronounced at the evaporation front (**Fig. 3a**, insets). This directly reflects the fact that $Pe_L > Pe_S$, meaning that the large particles diffuse more slowly away from the interface. However, as time progresses, this 'large-on-top' structure diminishes, resulting in a more homogeneous distribution across the film. These concentration gradients play a pivotal role in establishing the out-of-equilibrium state that drives the self-stratification within this mixture.

Upon increasing $\phi_{S,0}$ to 0.08 we observe a marked change in the stratification process. Once again, at the initial stages of evaporation, a uniform mixture is evident (**Fig. 3b**). However, after 1.9 h, a notable shift occurs: the peak intensity of the small particles advances closer to the evaporation front compared to the large particles (**Fig. 3b**, insets). This signifies small-on-top stratification, which continues to intensify over time. Here, the concentration gradient of the small particles becomes sufficiently significant to expel the large particles from the top of the drying coating — a phenomenon known as diffusiophoresis [13,18]. Upon further elevation of $\phi_{S,0}$ to 0.12, small-on-top stratification again occurs, yet featuring smaller concentration gradients compared to the film with $\phi_{S,0} = 0.08$ (**Fig. 3c**). We attribute this attenuation of the gradients to the higher initial concentration, which leads to an earlier onset of particle crowding and collective diffusion [25,51–53], and consequently lessens the prominence of diffusiophoresis. This is supported

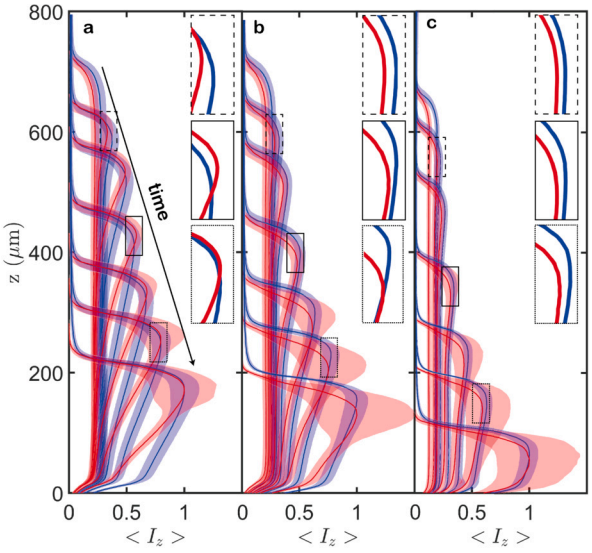

Fig. 3. Corrected median fluorescence intensity profiles of the small particles (55 nm, blue) and the large particles (360 nm, red) at different drying times. The shaded areas represent the 95% confidence interval. The insets show close-ups of the rectangular demarcated areas. (a) $\phi_{S,0} = 0.04$ and $\phi_{L,0} = 0.04$ after 0 h, 0.6 h, 1.1 h, 1.9 h, 2.3 h, 2.8 h and 3.2 h (from top to bottom). (b) $\phi_{S,0} = 0.08$ and $\phi_{L,0} = 0.04$ after 0 h, 0.6 h, 1.1 h, 1.9 h, 2.3 h 2.8 h and 3.2 h. (c) $\phi_{S,0} = 0.12$ and $\phi_{L,0} = 0.04$ after 0 h, 0.4 h, 1.0 h, 1.8 h, 2.4 h, 2.8 h and 3.2 h. The insets highlight how the volume fraction of the small particles influences self-stratification: from large-on-top (a) to small-on-top (b,c). The intensity fluctuations reflect the extent of phase separation, which manifests itself after ~2.5 h in all films.

by bulk viscosity measurements at the initial concentrations. The samples with $\phi_{S,0} = 0.04$ and $\phi_{S,0} = 0.08$ showed only slight increases in viscosity (η_r) by factors of 1.2 and 1.4, respectively, compared to the viscosity of pure formamide (η_0), indicating a dilute regime according to the Einstein relation: $\eta_r = \eta_0(1 + 2.5\phi)$. However, deviation from this relation can be found at $\phi_{S,0} = 0.12$, for which $\eta_r = 3.6$, suggesting that particle interactions, in addition to excluded volume effects, are contributing to the increased viscosity.

By fine-tuning $\phi_{S,0}$, we are thus capable of adjusting both the type and the extent of self-stratification. If we compare the final drying frame, we find that for $\phi_{S,0} = 0.04$, the dry film is homogeneous; for $\phi_{S,0} = 0.08$, small-on-top stratification with a layer thickness of around 30 μm is evident; and for $\phi_{S,0} = 0.12$, the stratification reduces to approximately 15 μm. In all films, around the 2.5-hour mark, the shaded area starts to expand (**Fig. 3**, 5th curve from the top). This shaded area represents the 95% confidence interval of the intensities in the xy images. Here, the expansion is not related to an increase in experimental error, but directly linked to the intensity fluctuations that occur due to phase separation. The phase separation initiates near the evaporation front, and in time extends over progressively greater distances. Additionally, its magnitude amplifies over time. Moreover, it persists throughout the drying process, and together with the self-stratification it dictates the composition of the fully dried film, as evidenced by observations in the physically created cross-sections (**Fig. 2**, **Fig. S3**).

3.3. Evolution of phase-separated domain size

As noted in previous sections, alongside self-stratification, phase separation distinctly governs the composition of the film. Hence, it is imperative to delve deeper into the phase separation phenomenon to gain a clearer understanding and effectively guide its impact on the ultimate composition. We initially concentrate on a time point at which phase separation is already abundant — 2.8 h into the evaporation process — and focus on the signal from the large particles. We focus on the large

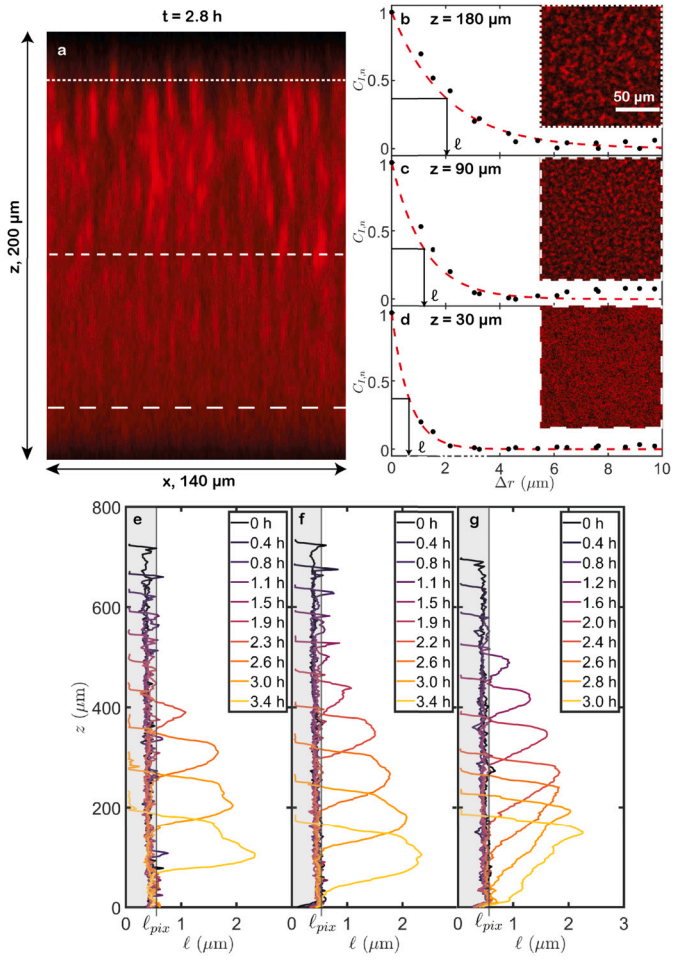

Fig. 4. Determination of the characteristic size (ℓ) of segregated zones within a drying binary suspension. (a) xz confocal fluorescence image of a film with $\phi_{S,0} = 0.08$ and $\phi_{L,0} = 0.04$ view after 2.8 h of evaporation. Distinct intensity fluctuations are visible at the top while the bottom is uniform. (b-d) Examples of spatial intensity correlation curves derived from the respective inset images, which depict xy confocal images at different depths indicated by the dashed lines in (a); the scale bar applies to all inset images. The red dashed lines are mono-exponential fits to the data. ℓ is the distance Δr where $C_{I,n} = 1/e$. (e-g) Evolution of ℓ across the depth of evaporating films with $\phi_{L,0} = 0.04$ and $\phi_{S,0} = 0.04$ (e), 0.08 (f), and 0.12 (g). The grey areas in (e-g) delineate the ℓ values below the detection limit of $\ell_{pix} \approx 0.5$ µm. Increasing $\phi_{S,0}$ alters the ℓ gradients, shifting it from large near the bottom and small at the evaporation front, to large at the evaporation and small near the bottom.

particle signal, because they are the minority spices. Therefore, we observe phase separated large particle domains in a continuous phase of small particles. Due to the higher concentration near the evaporation front, phase separation reaches its critical volume fraction earlier there. Consequently, we observe a distribution of large domains near the top, smaller domains further down, and no observable phase separation at the bottom (**Fig. 4a**). For these various depths, we can extract xy images from the 3D confocal dataset (**Fig. 4b-d**, insets). These images reveal lateral phase separation, which we quantify using a distance correlation function. This function compares the pixel intensity at a particular location with the intensity at a distance (Δr), via [54]:

$$C_I = \frac{< I(r) \cdot I(r+\Delta r) >}{< I(r) >< I(r+\Delta r) >} \tag{3}$$

The distance over which C_I decays is a measure for the characteristic domain size, which we denote by ℓ. We determine ℓ by first normalising the distance correlation function as $C_{I,n} = \frac{C_I(\Delta r)}{C_I(0)}$ and secondly fit $C_{I,n}$ to a mono-exponential function, and extracting the distance where the fit has decayed to $\frac{1}{e} \approx 0.368$. Using this procedure, we find that ℓ transitions from ~2.0 µm at z = 180 µm to ~1.2 µm at z = 90 µm and finally reaches ~0.5 µm for z = 30 µm (**Fig. 4b-d**). The latter is not physical in origin, since no clear phase separation is observable, but it is defined by the lateral pixel size (ℓ_{pix}), which is ~0.5 µm. For more examples of this spatial correlation on different samples, see **Fig. S6**. Note that these ℓ values closely resemble the characteristic length scales obtained from structure factor ($S(q)$) analysis used traditionally in phase separation studies (see **Fig. S7** for comparison). [55] We proceed with our distance correlation function as it provides a higher signal-to-noise ratio.

This distance correlation and fitting procedure are applicable to all samples across different time steps and depths, yielding varied ℓ values over time and at different z positions. For the film with $\phi_{0,S} = 0.04$ and $\phi_{0,L} = 0.04$, no discernible domains form within the first ~2.3 h of drying, indicated by a constant ℓ of ≈ 0.5 µm across the entire depth of the mixture (**Fig. 4e**, **Fig. S2a**, **video S3**). However, after 2.3 h, small domains begin to emerge near the evaporation front (z = 350-425 µm), reaching a maximum ℓ of ~ 1 µm. The relatively high Peclet numbers ($\gg 1$) (**Fig. S5** and **Tab. S1**) contribute to elevated concentrations near this front, leading to an earlier attainment of the critical volume fraction compared to deeper regions. As evaporation continues, the critical concentration for phase separation will also be attained within lower regions of the film, leading to a progressive increase in ℓ (after 2.6 hours, z = 175-275 µm). Interestingly, beyond 3 h, the largest ℓ values become skewed away from the evaporation interface (z = 75 µm), suggesting an influence of diffusiophoretic force that effectively 'push' domains towards the substrate (note the pronounced intensity gradients in **Fig. 3a**).

Raising $\phi_{S,0}$ to 0.08 prompts the first domain formation at 1.9 h (**Fig. 4f**, **video S2**), earlier than at $\phi_{S,0} = 0.04$. This is due to the higher $\phi_{S,0}$, accelerating the critical volume fraction attainment. At later time points, from 2.2 h onwards, we observe a further increment of ℓ surpassing 2 µm, and the domains disperse across a greater depth within the evaporating suspension. Elevating $\phi_{S,0}$ to 0.12 accelerates the onset of phase separation to just 1.5 h (**Fig. 4g**, **video S4**, **Fig. S2c**). These findings are in line with theoretical prediction, where a critical volume fraction needs to be crossed to obtain depletion fluctuation [33]. In contrast to the other films, the largest ℓ values remain concentrated near the evaporation front, while smaller domains are found in deeper regions. We hypothesize that the reduced concentration gradients in this film do not cause the domains to migrate to deeper regions (note the more shallow intensity profiles in **Fig. 3c**). Instead, the largest domains remain near their relative initial positions to the evaporation front, growing over time, while only at later time points the critical volume fraction is reached in deeper regions and phase separation is initiated.

3.4. Effects of the evaporation rate

Another means to delay the onset of domain formation is decreasing the evaporation speed. This effectively prevents the build-up of concentration gradients, thus approaching a quasi-equilibrium process that allows us to more effectively investigate phase separation without interference from the diffusiophoretic pathway. We achieve this by slightly increasing the pressure, resulting in a slower formamide evaporation. Under these conditions the particle diffusion will quickly level out the evaporation induced concentration gradients, as indicated by the relatively low $Pe_S = 2$ and $Pe_L = 16$ (**Fig. S5e** and **Tab. S1**). Indeed, both the small and large particle signals remain homogeneous throughout various measurements, and no vertical stratification is apparent (**Fig. 5**). Unlike previous experiments, phase-separated domains only start to appear after 10.7 hours of evaporation (**Fig. 5c**). However, this occurs when the film is ~70% of its initial height, which is slightly later than for the fast evaporating sample ≈ 75% (**Fig. 4g**).

The phase separated domains are initially absent at the evaporation interface, instead appearing in the bulk of the evaporating film, due to the similar concentration throughout the film. From there, the domains

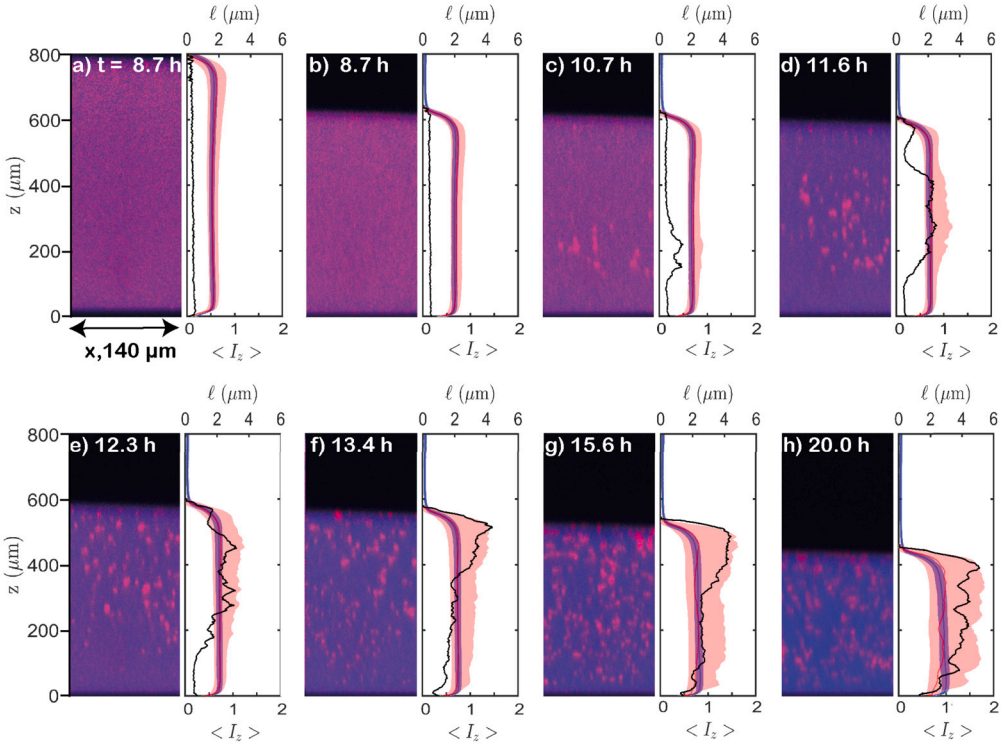

Fig. 5. xz confocal fluorescence images (left panels), fluorescence intensities (right panels, bottom axis), and characteristic domain size (right panels, top axis) throughout the depth of a slowly evaporating sample with initial volume fractions $\phi_{S,0}$ = 0.12 and $\phi_{L,0}$ = 0.04 at various time points as indicated. Slow drying clearly prevents stratification, delays the onset of phase separation, causes the phase domains to appear in an arbitrary location, and coarsen to high ℓ values over time.

gradually expand and propagate, eventually encompassing the entire sample depth (**Fig. 5d-f**). Nevertheless, a majority of the domains are concentrated near the evaporation front after 13.4 h (**Fig. 5e-g**). We attribute this to a slight density disparity between the solvent and the particles. While individual particles do not undergo creaming, larger clusters experience a drastically increased creaming velocity, driving them towards the evaporation interface. Another possibility is that due to the high Peclet numbers of these large clusters, they can not escape the incoming evaporation front.

After 20 h of evaporation, the domain size reaches values beyond 4 µm (**Fig. 5h**). In previous rapidly drying samples, ℓ was capped at a maximum of approximately 2 µm, likely due to earlier kinetic arrest, hindering further phase separation (**Fig. 4e-g**). Prolonged evaporation facilitates the formation of larger structures and potentially enables the manifestation of macroscopic phase separation. We support this by plotting the average domain size over time: for the samples with fast evaporation, ℓ plateaus around 2 µm, while the slowly evaporating sample features final structures of around 4 µm (**Fig. S8**). The drying rate thus offers a means to adjust the ultimate composition of the dried suspension.

3.5. Effect of the initial salt concentration

To delve deeper into the impact particle interactions on stratification and phase separation, we modify the particle interactions by adjusting the salt concentrations. Recent research indicates that elevating the background ion concentration significantly diminishes the diffusiophoretic effect, thereby modifying the stratification pattern [56,57]. Therefore, we synthesize charged particles with diameters of 45 nm and 430 nm (see the Materials and methods section). A charged initiator is used in these reactions providing a surface charge on both particles types. We make suspensions of these particles at specific salt concentrations: 1 mM, 10 mM, and 50 mM KCl. These KCl concentrations correspond to Debye screening lengths of 11 nm, 3.5 nm and 1.5 nm respectively (see Supplementary Material for calculations). This allows us to modulate the ionic interactions from significant electrostatic interactions (1 mM KCl) to shorter-ranged (10 mM KCl) to nearly hard-sphere repulsion (50 mM KCl). No significant particle aggregation due to electrostatic screening was observed at the initial salt concentrations, or even at higher concentrations (250 mM KCl), which will be reached later in the drying experiment (see **Fig. S9**). We set $\phi_{S,0}$ = 0.08 and $\phi_{L,0}$ = 0.04 and employ a relatively rapid evaporation process (**Tab. S1**, **Fig. 5Sf-h**), which previously produced well-defined stratified and phase-separated structures.

In the film with 1 mM KCl, already from the start of evaporation, self-stratification is visible (**Fig. 6a,b**). The top layer thickens locally as evaporation progresses (**Fig. 6c-e**). We do not observe any phase-separated domains at any time point (**Fig. 6a-f**, **Fig. S2d**), as opposed to earlier experiments. Raising the salt concentration to 10 mM KCl shows a comparable pattern to the previous film, albeit with a more pronounced concentration gradient (**Fig. 6g-i**). We observe distinct stratification of small particles on the surface, with a buildup of large particles below (**Fig. 6i-j**). After 2.2 h, within this accumulation of large particles, we also witness the emergence of phase-separated domains, akin to the films previously discussed (**Fig. 6k-l**, **Fig. S2e**). This suggests a combination of both segregation processes occurring simultaneously. Further reduction in the electrostatic interactions between the particles by increasing the salt concentration to 50 mM results in a more pronounced and earlier accumulation of both small and large particles near the evaporation front (**Fig. 6m-o**). Phase separation initiates early in the evaporation process, with small phase-separated features predominantly appearing near the evaporation front and persisting in this vicinity (**Fig. 6p-r**). Additionally, the stratification shifts from large-on-top stratification to small-on-top stratification during the evaporation process (**Fig. 6n-r**, **Fig. S2f**).

We hypothesize that the large differences between these films are due to the following effects: (1) At low salt concentration, the interaction distance between particles is significantly greater. This leads to

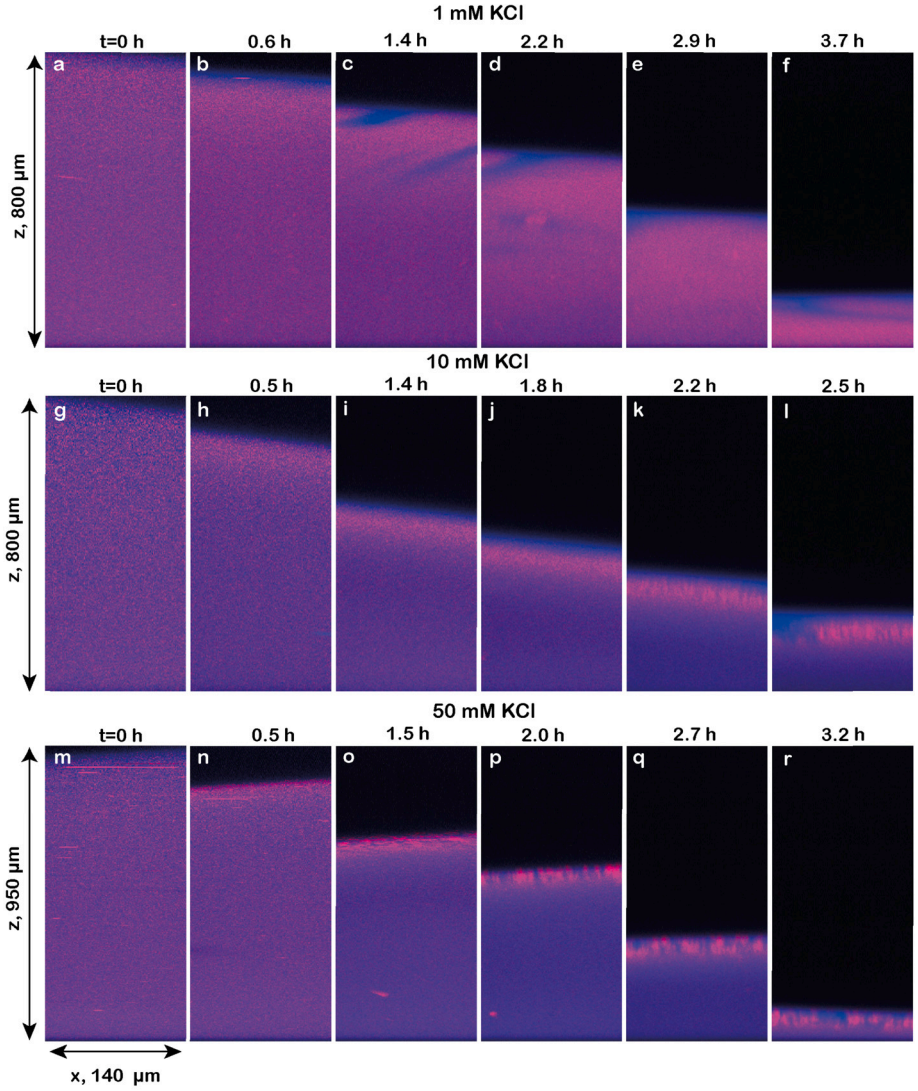

Fig. 6. xz confocal fluorescence images of an evaporating binary suspension with 420 nm particles (red) and 45 nm particles (blue) and an initial KCl concentration of (a-f) 1 mM, (g-l) 10 mM, and (m-r) 50 mM. All samples have $\phi_{S,0} = 0.08$ and $\phi_{l,0} = 0.04$. The salt concentration strongly influences the interaction distance between the particles, and consequently both self-stratification and phase separation.

an increase in the effective volume fraction, particularly affecting the small particles due to their larger ratio between their effective and hard sphere radii. Even small concentration gradients of these small particles can effectively push the large particles away from the interface, leading to more pronounced small-on-top stratification. Due to the pronounced stratification with smaller particles on top, the critical volume fraction for phase separation will no longer be reached in the bulk of the sample. (2) The effective particle size ratio increases with decreasing interaction range. As demonstrated previously, this factor significantly influences phase separation. Hence, for the higher salt concentrations, the phase boundary will be crossed, resulting in an earlier onset of phase separation. (3) A larger interaction distance leads to a higher collective diffusion [53], therefore no large concentration gradients build up. This fosters a more uniform particle distribution. Consequently, the critical concentration required for phase separation may not be attained near the evaporation front. For the lowest ionic strength, as the critical volume fraction approaches, the system becomes close to being kinetically trapped, thus preventing phase separation. (4) In addition to these factors, the salt concentration will increase as evaporation progresses. Although the salt concentration increases uniformly, since for the ions $Pe \ll 1$, it may alter the evolution of the described demixing processes. Overall, it is clear that changes in interaction distance, which are tunable through the salt concentration, significantly affect self-stratification and phase separation. This aspect offers an often overlooked control parameter for creating self-organizing films with desired composition.

4. Conclusions

In this study, we demonstrated diverse segregation patterns in drying binary colloidal mixtures. These patterns arise from self-stratification caused by concentration gradients that arise during evaporation due to high Peclet numbers. Additionally, phase separation occurs as a result of depletion interactions. Our work marks the first instance where these intertwined processes are elucidated and quantified during evaporation. This offers opportunities to fabricate self-segregating films with diverse compositions, since various parameters influence both phenomena significantly. (1) The particle size ratio: increasing the size ratio gradually enhances self-stratification and can also lead to phase separation. (2) Initial concentration: increasing the starting concentration of the small particles profoundly impacts stratification, shifting the structure from one with large particles on top to one with small particles on top. Additionally, this results in an earlier initiation of phase separation, and the location of the largest phase separated domains shifts towards the upper region of the film. (3) Evaporation rate: slowing down the drying

reduces self-stratification, while promoting larger phase-separated domains. Furthermore, the first phase domains form at a random depth, as opposed to at the evaporation interface in fast-drying films. (4) Colloidal interaction distance: this distance can be enlarged for charged colloids by decreasing the initial salt concentration, giving rise to sharp small-on-top stratification without phase separation. Conversely, small interaction distances lead to a more large-on-top stratified structure and robust phase separation. Intermediate distances yield intermediate states between these extremes. In this research, we have concentrated on factors with the most direct impact on self-stratification and phase separation [13,22,25,33,34,48,56,58]. However, future studies could investigate additional variables such as temperature [31], substrate chemistry and porosity, and viscosity [28,29]. The viscosity as a function of particle concentration exhibits a non-linear trend, indicating the importance of particle-particle interactions and collective behaviour at higher volume fractions. These volume fractions will also spatially and temporally change during evaporation. Therefore, examining micro-viscosity and collectivity during drying could provide a means to influence the demixing mechanisms. Additionally, particle–solvent interactions are an interesting factor to consider. Although we used formamide as the solvent to ensure refractive index matching, water-based systems would be more practical for industrial applications.

By adjusting these parameters, we can guide the composition of films during their drying process, starting from a homogeneous binary suspension. In the depth direction, self-stratification allows for the formation of layered or gradient structures, enabling functionally graded films. In the final dried film, we primarily observed small-on-top or homogeneous structures, with in some films a noticeable transition from large-on-top to small-on-top or to no stratification during drying. By using soft particles that can undergo wet sintering (coalescence), it may be possible to kinetically trap these large-on-top structures in an early stage. Also lateral heterogeneity may emerge through phase separation. This process may provide opportunities for creating additional multifunctional layers through the sedimentation or creaming of these domains during evaporation. This could explain the formation of three vertical layers observed in previous studies [22,27]. The formation of large particle or small particle domains at the film's surface [11,29] and in deeper regions may result from these depletion interactions [31]. Phase separation, originating from the depletion interactions can impact macroscopic properties of the dry film. Soft colloids undergoing phase separation might produce more resilient films, while segregated hard particles may yield stronger and stiffer films. Incorporating self-assembling rigid (non-)spherical colloids within these domains could facilitate structural colouring [59,60], with the outer phase serving as binder.

Given that both separation pathways are entropic in nature, these mechanisms can occur and tuned in a wide range of colloidal systems. To fully leverage the potential of both kinetic and phase separation size segregation pathways during the drying of binary colloidal films, a theoretical model is indispensable [40]. Our innovative, in-situ visualization offers a time-resolved understanding of both pathways, enabling comparison with predictive models. These predictive models afford complete control over these segregation pathways, facilitating the production of films with diverse compositions. This paves the way for sustainable, multifunctional colloidal-based coatings that can be applied in a single step.

CRediT authorship contribution statement

Ellard Hooiveld: Writing – original draft, Visualization, Validation, Software, Methodology, Investigation, Formal analysis, Data curation, Conceptualization. **Lisa Rijnders:** Writing – review & editing, Validation, Methodology, Investigation, Data curation, Conceptualization. **Berend van der Meer:** Writing – review & editing. **Jasper van der Gucht:** Writing – review & editing, Supervision, Funding acquisition, Conceptualization. **Joris Sprakel:** Writing – review & editing, Supervision, Funding acquisition, Conceptualization. **Hanne M. van der Kooij:** Writing – review & editing, Supervision, Methodology, Data curation, Conceptualization.

Funding

This work is part of the Advanced Research Center for Chemical Building Blocks, ARC-CBBC (project number: 2018.018.B.WUR.1), which is co-founded and co-financed by the Dutch Research Council (NWO) and the Netherlands Ministry of Economic Affairs and Climate Policy. BvdM acknowledges funding from the Dutch Research Council (NWO) through a Veni grant (Veni Grant No. VI.Veni.212.138).

Declaration of competing interest

The authors declare the following financial interests/personal relationships which may be considered as potential competing interests: Ellard Hooiveld reports financial support was provided by Advanced Research Center Chemical Building Blocks Consortium, ARC-CBBC. Berend van der Meer reports financial support was provided by Dutch Research Council (NWO). If there are other authors, they declare that they have no known competing financial interests or personal relationships that could have appeared to influence the work reported in this paper.

Appendix A. Supplementary material

Supplementary material related to this article can be found online at https://doi.org/10.1016/j.jcis.2024.10.102.

Data availability

All data needed to evaluate the conclusions in this paper are present in the paper or the Supplementary Materials. The raw data and analysis code that support this study are available upon reasonable request.

References

[1] H.M. van der Kooij, J. Sprakel, Watching paint dry; more exciting than it seems, Soft Matter 11 (32) (2015) 6353–6359.
[2] O. Cusola, S. Kivistö, S. Vierros, P. Batys, M. Ago, B.L. Tardy, L.G. Greca, M.B. Roncero, M. Sammalkorpi, O.J. Rojas, Particulate coatings via evaporation-induced self-assembly of polydisperse colloidal lignin on solid interfaces, Langmuir 34 (20) (2018) 5759–5771.
[3] R. Antonelli, R. Fokkink, N. Tomozeiu, J. Sprakel, T. Kodger, High-speed laser speckle imaging to unravel picoliter drop-on-demand to substrate interaction, Rev. Sci. Instrum. 92 (8) (2021) 083906.
[4] M. Yu, C. Le Floch-Fouéré, L. Pauchard, F. Boissel, N. Fu, X.D. Chen, A. Saint-Jalmes, R. Jeantet, L. Lanotte, Skin layer stratification in drying droplets of dairy colloids, Colloids Surf. A, Physicochem. Eng. Asp. 620 (2021) 126560.
[5] N.M. Eijkelboom, A.P. van Boven, I. Siemons, P.F. Wilms, R.M. Boom, R. Kohlus, M.A. Schutyser, Particle structure development during spray drying from a single droplet to pilot-scale perspective, J. Food Eng. 337 (2023) 111222.
[6] C. Le Floch-Fouéré, L. Pauchard, L. Lanotte, Crack patterns induced by auto-stratification in drying droplets of dairy proteins, in: IOP Food Physics, 2023.
[7] T.R. Palmer, H.M. van der Kooij, R. Abu Bakar, C.D. McAleese, M. Duewel, K. Greiner, P. Couture, M.K. Sharpe, J.L. Keddie, Diffusiophoresis-driven stratification in pressure-sensitive adhesive films from bimodal waterborne colloids, ACS Appl. Polym. Mater. (2023).
[8] R.B. Bjorklund, B. Liedberg, Electrically conducting composites of colloidal polypyrrole and methylcellulose, J. Chem. Soc., Chem. Commun. 16 (1986) 1293–1295.
[9] J.D. Tinkler, A. Scacchi, H.R. Kothari, H. Tulliver, M. Argaiz, A.J. Archer, I. Martín-Fabiani, Evaporation-driven self-assembly of binary and ternary colloidal polymer nanocomposites for abrasion resistant applications, J. Colloid Interface Sci. 581 (2021) 729–740.
[10] L. Goehring, J. Li, P.-C. Kiatkirakajorn, Drying paint: from micro-scale dynamics to mechanical instabilities, Philos. Trans. R. Soc. A, Math. Phys. Eng. Sci. 375 (2093) (2017) 20160161.
[11] Y. Dong, M. Argaiz, B. He, R. Tomovska, T. Sun, I. Martín-Fabiani, Zinc oxide superstructures in colloidal polymer nanocomposite films: enhanced antibacterial activity through slow drying, ACS Appl. Polym. Mater. 2 (2) (2020) 626–635.
[12] S. Hajeesaeh, S. Kariyo, N. Muensit, C. Daengngam, Self-stratifying particulate coating for robust superhydrophobic and latex-repellent surface, J. Environ. Treat. Tech. 8 (3) (2020) 1107–1111.

[13] M. Schulz, J. Keddie, A critical and quantitative review of the stratification of particles during the drying of colloidal films, Soft Matter 14 (30) (2018) 6181–6197.
[14] C.M. Cardinal, Y.D. Jung, K.H. Ahn, L. Francis, Drying regime maps for particulate coatings, AIChE J. 56 (11) (2010) 2769–2780.
[15] R. Trueman, E. Lago Domingues, S. Emmett, M. Murray, A. Routh, Auto-stratification in drying colloidal dispersions: a diffusive model, J. Colloid Interface Sci. 377 (jul 2012) 207–212.
[16] A. Fortini, I. Martín-Fabiani, J.L. De La Haye, P.-Y. Dugas, M. Lansalot, F. D'agosto, E. Bourgeat-Lami, J.L. Keddie, R.P. Sear, Dynamic stratification in drying films of colloidal mixtures, J. Colloid Interface Sci. 116 (11) (2016) 118301.
[17] A. Fortini, R.P. Sear, Stratification and size segregation of ternary and polydisperse colloidal suspensions during drying, Langmuir 33 (19) (2017) 4796–4805.
[18] R.P. Sear, P.B. Warren, Diffusiophoresis in nonadsorbing polymer solutions: the Asakura-Oosawa model and stratification in drying films, Phys. Rev. E 96 (6) (2017) 062602.
[19] J. Zhou, Y. Jiang, M. Doi, Cross interaction drives stratification in drying film of binary colloidal mixtures, Phys. Rev. Lett. 118 (10) (2017) 108002.
[20] M. Schulz, R.W. Smith, R.P. Sear, R. Brinkhuis, J.L. Keddie, Diffusiophoresis-driven stratification of polymers in colloidal films, ACS Macro Lett. 9 (9) (2020) 1286–1291.
[21] C.R. Rees-Zimmerman, A.F. Routh, Stratification in drying films: a diffusion–diffusiophoresis model, J. Fluid Mech. 928 (2021).
[22] W. Liu, A.J. Carr, K.G. Yager, A.F. Routh, S.R. Bhatia, Sandwich layering in binary nanoparticle films and effect of size ratio on stratification behavior, J. Colloid Interface Sci. 538 (2019) 209–217.
[23] I. Martín-Fabiani, A. Fortini, J. Lesage de la Haye, M.L. Koh, S.E. Taylor, E. Bourgeat-Lami, M. Lansalot, F. D'agosto, R.P. Sear, J.L. Keddie, ph-switchable stratification of colloidal coatings: surfaces "on demand", ACS Appl. Mater. Interfaces 8 (50) (2016) 34755–34761.
[24] A.K. Atmuri, S.R. Bhatia, A.F. Routh, Autostratification in drying colloidal dispersions: effect of particle interactions, Langmuir 28 (5) (2012) 2652–2658.
[25] E. Hooiveld, H.M. van der Kooij, M. Kisters, T.E. Kodger, J. Sprakel, J. van der Gucht, In-situ and quantitative imaging of evaporation-induced stratification in binary suspensions, J. Colloid Interface Sci. 630 (Pt B) (2022) 666–675.
[26] A. Samanta, R. Bordes, On the effect of particle surface chemistry in film stratification and morphology regulation, Soft Matter 16 (27) (2020) 6371–6378.
[27] A.J. Carr, C.R. Rees-Zimmerman, B. Zheng, A.F. Routh, S.R. Bhatia, Experimental and numerical investigation of stratification regimes in drying polystyrene and silica nanoparticle films: implications for evaporative self-assembly of colloidal particles, ACS Appl. Nano Mater. (2024).
[28] M. Schulz, R. Brinkhuis, C. Crean, R. Sear, J. Keddie, Suppression of self-stratification in colloidal mixtures with high péclet numbers, Soft Matter 18 (13) (2022) 2512–2516.
[29] T.J. Murdoch, B. Quienne, M. Argaiz, R. Tomovska, E. Espinosa, F. D'agosto, M. Lansalot, J. Pinaud, S. Caillol, I. Martín-Fabiani, One step closer to coatings applications utilizing self-stratification: effect of rheology modifiers, ACS Appl. Polym. Mater. 5 (8) (2023) 6672–6684.
[30] J.H. Jeong, Y.K. Lee, K.H. Ahn, Stratification mechanism in the bidisperse colloidal film drying process: evolution and decomposition of normal stress correlated with microstructure, Langmuir 37 (46) (2021) 13712–13728.
[31] E. Hooiveld, M. Dols, J. van der Gucht, J. Sprakel, H.M. van der Kooij, Quantitative imaging methods for heterogeneous multi-component films, Soft Matter (2023).
[32] W. Liu, J. Midya, M. Kappl, H.-J. Butt, A. Nikoubashman, Segregation in drying binary colloidal droplets, ACS Nano 13 (5) (2019) 4972–4979.
[33] M. Dijkstra, R. van Roij, R. Evans, Phase diagram of highly asymmetric binary hard-sphere mixtures, Phys. Rev. E 59 (5) (1999) 5744.
[34] A. Dinsmore, A. Yodh, D. Pine, Phase diagrams of nearly-hard-sphere binary colloids, Phys. Rev. E 52 (4) (1995) 4045.
[35] J.S. Van Duijneveldt, A. Heinen, H. Lekkerkerker, Phase separation in bimodal dispersions of sterically stabilized silica particles, Europhys. Lett. 21 (3) (1993) 369.
[36] P. Bartlett, R. Ottewill, Geometric interactions in binary colloidal dispersions, Langmuir 8 (8) (1992) 1919–1925.
[37] G. Mansoori, N.F. Carnahan, K. Starling, T. Leland Jr, Equilibrium thermodynamic properties of the mixture of hard spheres, J. Chem. Phys. 54 (4) (1971) 1523–1525.
[38] M.D. Haw, M. Gillie, W.C.K. Poon, Effects of phase behavior on the drying of colloidal suspensions, Langmuir 18 (5) (2002) 1626–1633.
[39] C. Schaefer, J.J. Michels, P. van der Schoot, Structuring of thin-film polymer mixtures upon solvent evaporation, Macromolecules 49 (18) (2016) 6858–6870.
[40] C. Schaefer, J.J. Michels, P. van der Schoot, Dynamic surface enrichment in drying thin-film binary polymer solutions, Macromolecules 50 (15) (2017) 5914–5919.
[41] H. Diestra-Cruz, E. Bukusoglu, N.L. Abbott, A. Acevedo, Hierarchical microstructures formed by bidisperse colloidal suspensions within colloid-in-liquid crystal gels, ACS Appl. Mater. Interfaces 7 (13) (2015) 7153–7162.
[42] W. Brouwer, The preparation of small polystyrene latex particles, J. Appl. Polym. Sci. 38 (7) (1989) 1335–1346.
[43] M. Egen, R. Zentel, Surfactant-free emulsion polymerization of various methacrylates: towards monodisperse colloids for polymer opals, Macromol. Chem. Phys. 205 (11) (2004) 1479–1488.
[44] T.E. Kodger, R.E. Guerra, J. Sprakel, Precise colloids with tunable interactions for confocal microscopy, Sci. Rep. 5 (2015) 14635.
[45] R.D. Deegan, O. Bakajin, T.F. Dupont, G. Huber, S.R. Nagel, T.A. Witten, Capillary flow as the cause of ring stains from dried liquid drops, Nature 389 (6653) (1997) 827–829.
[46] R.P. Sear, Stratification of mixtures in evaporating liquid films occurs only for a range of volume fractions of the smaller component, J. Chem. Phys. 148 (13) (2018) 134909.
[47] D. Makepeace, A. Fortini, A. Markov, P. Locatelli, C. Lindsay, S. Moorhouse, R. Lind, R. Sear, J. Keddie, Stratification in binary colloidal polymer films: experiment and simulations, Soft Matter 13 (39) (2017) 6969–6980.
[48] H.M. Coureur, T. Petithory, A. Airoudj, L. Josien, A. Trajcheva, R. Tomovska, A. Chemtob, Stratified and gradient films by evaporation-induced stratification of bimodal latexes. Potential of confocal and scanning electron microscopy for compositional depth profiling, Polymer 269 (2023) 125752.
[49] J. Keddie, A.F. Routh, Fundamentals of Latex Film Formation: Processes and Properties, Springer Science & Business Media, 2010.
[50] A.F. Routh, Drying of thin colloidal films, Rep. Prog. Phys. 76 (4) (2013) 046603.
[51] A. Van Blaaderen, J. Peetermans, G. Maret, J. Dhont, Long-time self-diffusion of spherical colloidal particles measured with fluorescence recovery after photobleaching, J. Chem. Phys. 96 (6) (1992) 4591–4603.
[52] B. Sobac, S. Dehaeck, A. Bouchaudy, J.-B. Salmon, Collective diffusion coefficient of a charged colloidal dispersion: interferometric measurements in a drying drop, Soft Matter 16 (35) (2020) 8213–8225.
[53] J. Appell, G. Porte, E. Buhler, Self-diffusion and collective diffusion of charged colloids studied by dynamic light scattering, J. Phys. Chem. B 109 (27) (2005) 13186–13194.
[54] H.M. Van Der Kooij, R. Fokkink, J. Van Der Gucht, J. Sprakel, Quantitative imaging of heterogeneous dynamics in drying and aging paints, Sci. Rep. 6 (1) (2016) 34383.
[55] P.J. Lu, E. Zaccarelli, F. Ciulla, A.B. Schofield, F. Sciortino, D.A. Weitz, Gelation of particles with short-range attraction, Nature 453 (7194) (2008) 499–503.
[56] C.R. Rees-Zimmerman, A.F. Routh, Stratification in drying films: diffusiophoresis driven by nanoparticles and their counterions, IMA J. Appl. Math. (2024) hxae015.
[57] C.R. Rees-Zimmerman, D.H. Chan, S.P. Armes, A.F. Routh, Diffusiophoresis of latex driven by anionic nanoparticles and their counterions, J. Colloid Interface Sci. 649 (2023) 364–371.
[58] M. Schulz, C. Crean, R. Brinkhuis, R. Sear, J. Keddie, Determination of parameters for self-stratification in bimodal colloidal coatings using Raman depth profiling, Prog. Org. Coat. 157 (2021) 106272.
[59] J.M. Clough, E. Guimard, C. Rivet, J. Sprakel, T.E. Kodger, Photonic paints: structural pigments combined with water-based polymeric film-formers for structurally colored coatings, Adv. Opt. Mater. 7 (15) (2019) 1900218.
[60] A.G. Dumanli, H.M. Van Der Kooij, G. Kamita, E. Reisner, J.J. Baumberg, U. Steiner, S. Vignolini, Digital color in cellulose nanocrystal films, ACS Appl. Mater. Interfaces 6 (15) (2014) 12302–12306.